Available online at www.sciencedirect.com
SCIENCE DIRECT®
ELSEVIER
International Journal of Mechanical Sciences 47 (2005) 666–686
International Journal of MECHANICAL SCIENCES
www.elsevier.com/locate/ijmecsci

A constitutive model for transversely isotropic foams, and its application to the indentation of balsa wood

V.L. Tagarielli[a], V.S. Deshpande[a], N.A. Fleck[a,*], C. Chen[b]

[a]*Engineering Department, Cambridge University, Trumpington Street, CB2 1PZ Cambridge, UK*
[b]*State Key Laboratory, Xian Jiaotong University, Xian 710049, PR China*

Received 3 August 2004; received in revised form 11 November 2004; accepted 11 November 2004
Available online 2 April 2005

Abstract

An elastic-plastic constitutive model for transversely isotropic compressible solids (foams) has been developed. A quadratic yield surface with four parameters and one hardening function is proposed. Associated plastic flow is assumed and the yield surface evolves in a self-similar manner calibrated by the uniaxial compressive (or tensile) response of the cellular solid in the axial direction. All material constants in the model (elastic and plastic) can be determined from a combination of a total of four uniaxial and shear tests. The model is used to predict the indentation response of balsa wood to a conical indenter. For the three cone angles considered in this study, very good agreement is found between the experimental measurements and the finite element (FE) predictions of the transversely isotropic cellular solid model. On the other hand, an isotropic foam model is shown to be inadequate to capture the indentation response.

Keywords: Constitutive model; Transversely isotropic; Cellular solids; Balsa wood; Finite element

1. Introduction

A wide range of natural and man-made cellular solids are transversely isotropic in mechanical properties. For example, if a sample of wood is cut at a sufficient distance from the centre of the tree that the curvature of the growth rings can be neglected, its properties are transversely

*Corresponding author. Tel.: +44 1223 332650; fax: +44 1223 332662.
E-mail address: naf1@eng.cam.ac.uk (N.A. Fleck).

0020-7403/$ - see front matter
doi:10.1016/j.ijmecsci.2004.11.010

isotropic in the plane perpendicular to the axis of the tree trunk [1]. Similarly, a variety of new lattice cores, such as the Octet truss [2], the pyramidal core [3] and the square-honeycomb [4] exhibit transverse isotropy. The aim of this study is to develop an elastic-plastic constitutive model for a transversely isotropic compressible continuum and validate it by performing conical indentation experiments on the transversely isotropic solid, balsa wood.

A variety of models have been developed for the "yield surface" of anisotropic foams (or compressible solids). Gibson and Ashby [1] extended the yield surface proposed by Triantafillou and Gibson [5] for isotropic foams to cellular solids with an orthotropic symmetry. On similar lines, Deshpande et al. [2] developed a quadratic yield surface for compressible orthotropic solids by extending the Hill [6] quadratic yield criterion for incompressible solids with orthotropic symmetry. The proposed model [2] has seven plasticity constants that need to be set either by experimentation or by numerical calculations of the plastic properties of the anisotropic foam. With suitable choices of the seven parameters, this criterion reduces to the Deshpande and Fleck [7] model for isotropic foams. Deshpande et al. [2] applied this yield criterion to the cubic Octet truss lattice material. Comparisons between the numerically calculated collapse surfaces of the Octet truss and predictions of the proposed quadratic yield criterion revealed that the compressible version [2] of the Hill [6] model is unable to capture yield behaviour of the Octet truss under arbitrary states of stress.

Recently, Xue and Hutchinson [8] have proposed a continuum constitutive model for compressible orthotropic metallic sandwich cores. Their quadratic yield surface model is similar to that proposed by Deshpande et al. [2] but has three additional plasticity parameters which more accurately describe the mean stress dependence of the orthotropic solids. Xue and Hutchinson [8] calibrated their model for the pyramidal and square-honeycomb lattice cores and employed it to predict the quasi-static response of clamped pyramidal and square-honeycomb core sandwich beams. Comparisons with full three-dimensional finite element (FE) simulations indicated that the model is adequate when calibrated by the stress versus strain response of the lattice core in the appropriate direction. The orthotropic compressible constitutive models of Deshpande et al. [2] and Xue and Hutchinson [8] are sophisticated and require at-least six stress versus strain histories to calibrate them. Moreover, experimental validation of their models is lacking.

The aim of this study is to develop a simpler transversely isotropic compressible constitutive model that is expected to suffice for a number of natural and man-made cellular solids. The outline of the paper is as follows. First, the transversely isotropic model is presented. Next, the mechanical properties of balsa wood are measured and these experiments used to calibrate the proposed model. Finally, conical indentation experiments on balsa wood are reported, and are compared with FE predictions using the transversely isotropic compressible constitutive model.

2. Yield behaviour of transversely isotropic solids

Consider a transversely isotropic compressible solid and choose the Cartesian axes of reference (x_1, x_2, x_3) such that the axes $x_1 - x_2$ lay in the isotropic plane. Decompose the total strain ε_{ij} into an elastic part ε^e_{ij} and a plastic part ε^p_{ij} such that

$$\dot{\varepsilon}_{ij} = \dot{\varepsilon}^e_{ij} + \dot{\varepsilon}^p_{ij}, \tag{1}$$

where the overdot indicates differentiation with respect to time. The elastic properties of such a solid (where x_3 is an axis of six-fold symmetry) can be written in terms of five "engineering" elastic constants; 2 Young's moduli in the 1 and 3 directions, E_{11} and E_{33}, two Poisson's ratios defined as $v_{12} = -\varepsilon^e_{22}/\varepsilon^e_{11}$ and $v_{13} = -\varepsilon^e_{33}/\varepsilon^e_{11}$ for uniaxial loading in the directions 1 and 3 and the shear modulus E_{13} in the $x_1 - x_3$ plane. Then the elastic strain ε^e_{ij} is related to the macroscopic Cauchy stress σ_{ij} by

$$\begin{bmatrix} \varepsilon^e_{11} \\ \varepsilon^e_{22} \\ \varepsilon^e_{33} \\ 2\varepsilon^e_{12} \\ 2\varepsilon^e_{23} \\ 2\varepsilon^e_{31} \end{bmatrix} = \mathbf{S}\boldsymbol{\sigma} = \begin{bmatrix} 1/E_1 & -v_{12}/E_1 & -v_{13}/E_3 & & & \\ -v_{12}/E_1 & 1/E_1 & -v_{13}/E_3 & & & \\ -v_{13}/E_3 & -v_{13}/E_3 & 1/E_3 & & & \\ & & & 2(1+v_{12})/E_1 & & \\ & & & & 1/E_{13} & \\ & & & & & 1/E_{13} \end{bmatrix} \begin{bmatrix} \sigma_{11} \\ \sigma_{22} \\ \sigma_{33} \\ \sigma_{12} \\ \sigma_{23} \\ \sigma_{31} \end{bmatrix}, \tag{2}$$

where $\mathbf{S}$ is the elastic compliance tensor.

A plastic yield criterion for transversely isotropic solids can be stated as

$$\Phi = \bar{\sigma} - Y \leqslant 0, \tag{3}$$

where $\bar{\sigma}$ is an equivalent stress to be defined and Y is the current yield strength. We proceed to specify the effective stress $\bar{\sigma}$. Following Lubliner [9] we define

$$\begin{aligned} \bar{\sigma}^2 \equiv \boldsymbol{\sigma}^{\mathrm{T}}\mathbf{P}\boldsymbol{\sigma} = {} & B^2(\sigma^2_{11} + \sigma^2_{22}) + \sigma^2_{33} - C^2\sigma_{11}\sigma_{22} \\ & - D^2\sigma_{33}(\sigma_{11} + \sigma_{22}) + E^2\sigma^2_{12} + F^2(\sigma^2_{32} + \sigma^2_{13}) \end{aligned} \tag{4}$$

such that $\bar{\sigma} = |\sigma_{33}|$ for uniaxial loading in the 3 direction. The plasticity matrix $\mathbf{P}$ is given by

$$\mathbf{P} = \begin{bmatrix} B^2 & -C^2/2 & -D^2/2 & & & \\ -C^2/2 & B^2 & -D^2/2 & & & \\ -D^2/2 & -D^2/2 & 1 & & & \\ & & & E^2 & & \\ & & & & F^2 & \\ & & & & & F^2 \end{bmatrix}. \tag{5}$$

It has the same symmetries as $\mathbf{S}$ and is specified in terms of the five constants B to F which characterise the plastic anisotropy of the foam. Note that the yield criterion (3) can be reduced to a variety of well developed elastic-plastic models, including the von Mises model and the Deshpande and Fleck [7] model for isotropic metallic foams. For example, with the choice

$$B = 1, \quad C^2 = D^2 = \frac{1 - 2\alpha^2/9}{1 + \alpha^2/9}, \quad E^2 = F^2 = \frac{3}{1 + \alpha^2/9}. \tag{6}$$

$\bar{\sigma}$ reduces to the effective stress measure proposed by Deshpande and Fleck [7] for isotropic metallic foams, while the von Mises yield criterion is recovered by setting

$$B = C = D = 1, \quad E^2 = F^2 = 3. \tag{7}$$

2.1. Associated flow rule

The plastic strain rate $\dot{\varepsilon}^p_{ij}$ is assumed to be normal to the yield surface (associated flow) and is given by

$$\dot{\varepsilon}^p_{ij} = \frac{1}{H}\frac{\partial \Phi}{\partial \sigma_{ij}}\frac{\partial \Phi}{\partial \sigma_{kl}}\breve{\sigma}_{kl}, \tag{8}$$

where H is the hardening modulus and $\breve{\sigma}_{ij}$ is the Jaumann stress rate. The Jaumann stress rate has been used here to ensure objectivity to rigid body rotation. For continued plastic flow, the consistency relation reads

$$\dot{\Phi} = 0 = \frac{\partial \Phi}{\partial \sigma_{ij}}\breve{\sigma}_{ij} + \frac{\partial \Phi}{\partial Y}\dot{Y}. \tag{9}$$

Upon noting from Eq. (3) that $\partial\Phi/\partial Y = -1$, the consistency relation reduces to

$$\frac{\partial \Phi}{\partial \sigma_{ij}}\breve{\sigma}_{ij} = \dot{Y} \tag{10}$$

and thus substituting Eq. (10) in the flow rule (8) we obtain

$$\dot{\varepsilon}^p_{ij} = \frac{\dot{Y}}{H}\frac{\partial \Phi}{\partial \sigma_{ij}}. \tag{11}$$

Now introduce an equivalent strain rate $\dot{\bar{\varepsilon}}$ which is the plastic work rate conjugate to $\bar{\sigma}$,

$$\bar{\sigma}\dot{\bar{\varepsilon}} = \sigma_{ij}\dot{\varepsilon}^p_{ij} \tag{12}$$

such that the equivalent strain rate $\dot{\bar{\varepsilon}} = |\dot{\varepsilon}_{33}|$ for uniaxial loading in the 3 direction. Substituting Eq. (11) into Eq. (12) and employing the observation that Φ is homogeneous of degree 1 in stress, we obtain

$$\dot{\bar{\varepsilon}} = \frac{\dot{Y}}{H} = \frac{\dot{\bar{\sigma}}}{H} \tag{13}$$

and thus the flow rule (11) is re-written as

$$\dot{\varepsilon}^p_{ij} = \dot{\bar{\varepsilon}}\frac{\partial \Phi}{\partial \sigma_{ij}}. \tag{14}$$

To summarise, we have given definitions for the yield criterion and the flow rule. It now remains to specify the hardening modulus H. In general, H is homogenous and of degree zero in stress rate. Here, we choose to restrict our definition of H to depend only on the accumulated plastic strain $\bar{\varepsilon}$. Thus, with this assumption the yield surface evolves in a geometrically self-similar manner.

2.2. Calibration of the constitutive model

The constitutive law requires the specification of 10 coefficients and one hardening function: five for elasticity (E_{11}, E_{33}, v_{12}, v_{13} and E_{13}), five for plasticity (B to F) and $H(\bar{\varepsilon})$. In principle data from four sets of stress versus strain histories are required to calibrate the model. Uniaxial stressing (tension or compression) in the 3 and 1 (or 2) direction provides the moduli E_{33} and E_{11} along with Poisson's ratios v_{13} and v_{12} while the shear modulus E_{13} can be obtained via a shear test in the 1–3 plane. An additional shear test in the 1–2 direction will be required to calibrate the plasticity constant as described below; this shear test can also be used to obtain the Poisson's ratio v_{12} through the relation

$$E_{12} = \frac{E_{11}}{2(1+v_{12})}.$$

Each of the tests described above generates information for determining the constants B to F and $H(\bar{\varepsilon})$. Under uniaxial loading in the 3 direction, the equivalent stress $\bar{\sigma} = |\sigma_{33}|$ and strain $\bar{\varepsilon} = |\varepsilon^p_{33}|$ and thus hardening modulus curve $H(\bar{\varepsilon})$ is the slope of the uniaxial Cauchy stress $|\sigma_{33}|$ versus logarithmic plastic strain $|\varepsilon^p_{33}|$ curve for uniaxial compression (or tension) in the 3 direction. Also from the definitions of the yield function (3) and the effective stress (4) we have

$$B^2 = \frac{Y_{33}^2}{Y_{11}^2} = \frac{Y_{33}^2}{Y_{22}^2}, \quad E^2 = \frac{Y_{33}^2}{Y_{12}^2} \quad \text{and} \quad F^2 = \frac{Y_{33}^2}{Y_{23}^2} = \frac{Y_{33}^2}{Y_{31}^2}, \tag{15}$$

where Y_{ij} denote the stress components at the onset of yield ($\bar{\varepsilon} = 0$). It now remains to specify the constants C and D. These constants are obtained from the plastic Poisson's ratios v^p_{21} and $v^p_{31} = v^p_{32}$. Recall that the plastic Poisson's ratio v^p_{ij} is defined as

$$v^p_{ij} = -\frac{\dot{\varepsilon}^p_{jj}}{\dot{\varepsilon}^p_{ii}} \quad \text{(no summation on } i,j) \tag{16}$$

for uniaxial compression in the i direction. The flow rule (14) dictates that

$$C^2 = 2B^2 v^p_{21} \quad \text{and} \quad D^2 = v^p_{31} = v^p_{32} \tag{17}$$

and so C and D are obtained via the measurements of v^p_{21} and v^p_{31}, respectively. Thus four sets of stress versus strain histories suffice to completely calibrate the transversely isotropic model: (i) uniaxial compression (or tension) in the 3 direction, (ii) uniaxial compression (or tension) in either the 1 or 3 direction, (ii) shearing in the 1–3 direction and (iv) shearing in the 1–2 direction.

This model has been implemented into the commercial FE package ABAQUS via the user material subroutine interface UMAT, see Chen et al. [10] for details of the implementation procedure.

3. Balsa wood as a transversely isotropic cellular solid

Balsa wood is unique among commercial woods in the fact that its density is exceptionally low and varies over a wide range depending on the age of the tree and where it is grown. Densities can vary from 40 to 320 kg m^{-3}, although most commercial balsa falls within the range 80–250 kg m^{-3}.

The main current commercial applications of balsa include thermal insulation for refrigerated ships, a floatation aid in lifeboats, a lightweight core material for sandwich cores and for packaging applications.

The cellular microstructure and mechanical properties of balsa wood have been analysed by Easterling et al. [11]. They concluded that for most practical purposes, balsa wood can be thought of as transversely isotropic with the isotropic plane being perpendicular to the axis of the tree. Thus, balsa wood is an ideal candidate for the experimental validation of the transversely isotropic foam model proposed in Section 2. Here, we first review the microstructure of balsa wood and measure its mechanical properties both to confirm the in-plane isotropy and to calibrate the plasticity model.

3.1. Microstructure

A section through the trunk of a balsa tree showing the axial (z), radial (r) and tangential (θ) directions is sketched in Fig. 1a. On the scale of millimetres, balsa wood is a cellular solid made up of long, hexagonal-prismatic cells, with pointed ends and an aspect ratio of about 16:1 as shown in Fig. 1b. These long cells are subdivided occasionally by transverse walls. Blocks of such grains are separated by narrower rays in which cells are smaller and of different shape. The entire structure is penetrated by large sap channels running parallel to the axis of tree (see micrograph in Fig. 6b). Typical dimensions of the cells are indicated in Fig. 1b. Over the entire cross-section of a tree trunk, growth rings forming cylindrical surfaces normal to the rays are visible to the naked eye but are too diffuse to appear on micrographs.

3.2. Materials

Commercial balsa wood (trade name ProBalsa® LD7) was procured from DIAB[1] in the form of 16 mm thick sheets. The main commercial application of these balsa wood sheets manufactured by DIAB is cores of sandwich panels for marine applications. The sheets were manufactured by gluing together blocks of balsa wood. This assembly is then sliced into the 16 mm thick sheets such that the thickness direction of the sheet is parallel to the axis of the balsa tree trunk (z direction). The nominal density of the balsa wood sheets as quoted by the manufacturer was $90\,\mathrm{kg\,m^{-3}}$. However, the density of the wood varied typically from 70 to $150\,\mathrm{kg\,m^{-3}}$ across the different blocks comprising the sheet.

3.3. Test protocol

Cuboidal compression and shear test specimens were cut from the balsa wood sheets with a fresh razor blade. Recall that the balsa wood sheets were manufactured by gluing together balsa wood blocks. Care was taken to ensure that the specimens did not span these glued interfaces so that the measured properties represent true balsa wood properties. Unless otherwise specified, the cuboidal specimen dimensions are quoted as $L_r \times L_\theta \times L_z$, where L_r, L_θ and L_z are the side lengths in the radial, tangential and axial directions, respectively.

[1]DIAB Technologies—315 Seahawk Drive, DeSoto, TX 75115, USA.

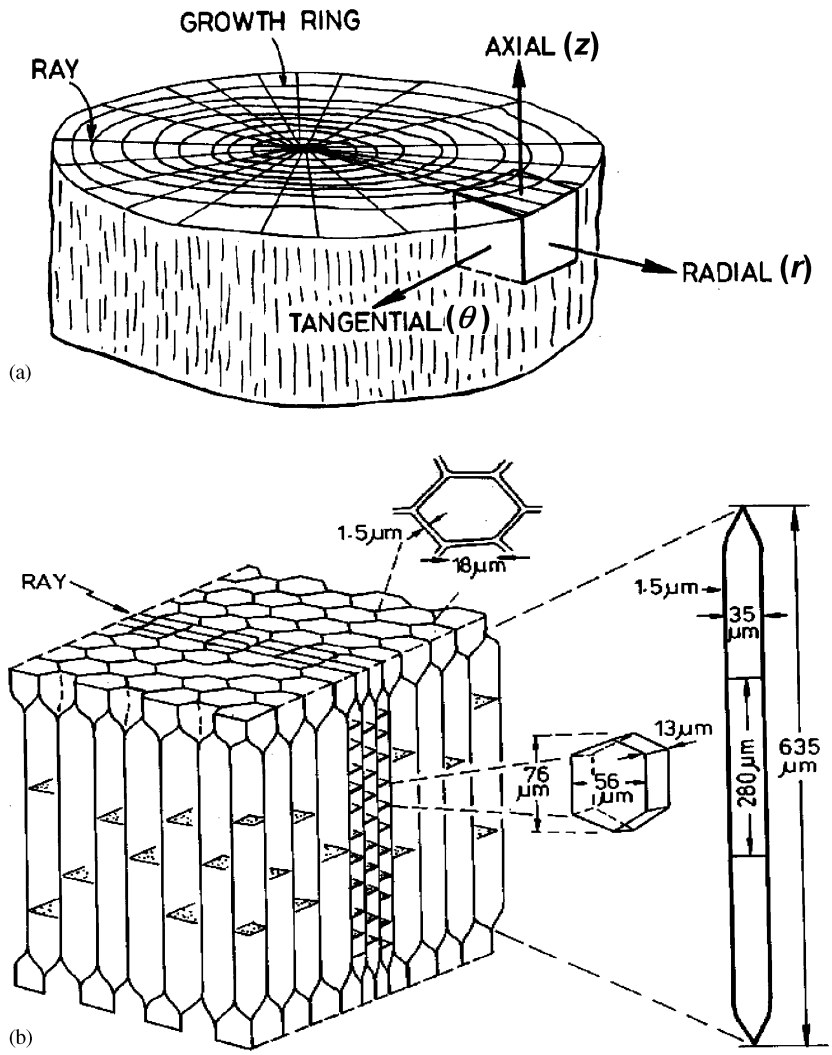

Fig. 1. (a) A section through the trunk of a balsa tree showing the axial (z), radial (r) and tangential (θ) directions and (b) a model for the cellular structure of balsa wood with typical cell dimensions marked. (Reproduced from Gibson and Ashby [1]).

3.3.1. Compression tests

Compression experiments were conducted in a screw driven test machine with load measured via the load cell of the test machine and compressive strain deduced by measuring the displacement of the compression platens using a laser extensometer. All tests were conducted at a nominal strain rate of $10^{-3}\,s^{-1}$. The platens were lubricated with a silicone spray to reduce frictional effects.

In order to determine the plastic Poisson's ratio, the specimens were compressed in increments of approximately 5% axial plastic strain and the specimen width was measured at three points along the height of the specimen using a micrometer. On the other hand, to accurately measure

the Young's moduli and the elastic Poisson's ratios, 90° strain gauge rosettes were employed to measure the initial strains in a few compression specimens.

Uniaxial compression tests in 4 directions were conducted in order to characterise the anisotropy of the material.

(i) Axial compression (σ_{zz} versus ε_{zz}) tests were conducted on $30 \times 30 \times 16\,\text{mm}^3$ specimens.
(ii) Radial (σ_{rr} versus ε_{rr}) compression tests were conducted on $20 \times 30 \times 16\,\text{mm}^3$ specimens.
(iii) Tangential ($\sigma_{\theta\theta}$ versus $\varepsilon_{\theta\theta}$) compression tests were conducted on $30 \times 20 \times 16\,\text{mm}^3$ specimens.
(iv) Compression tests in the $(r-\theta)$ plane in a direction at 45° to the r and θ directions. Cuboidal specimens $30 \times 20 \times 16\,\text{mm}^3$ were used with the compressive direction corresponding to the 20 mm side.

Note that the growth rings visible on the balsa wood sheets were used to locate the r and θ directions.

3.3.2. Shear tests

Single lap shear tests were conducted on cuboidal balsa wood specimens as per the ASTM standard C273-94 [12] for shear tests on sandwich cores. The specimens were glued to steel shear platens with an epoxy-based glue. Load measured via the load cell of the screw-driven test machine was used to determine shear stress, while the relative displacement of the platens, measured via a laser extensometer, was used to define the shear strain. All tests were conducted at a nominal shear strain rate of $10^{-3}\,\text{s}^{-1}$. In order to measure accurately the shear moduli, strain gauge rosettes were employed in a few shear test specimens. Shear tests were conducted in 3 directions using the following specimen dimensions:

(i) Cuboidal specimens $160 \times 20 \times 16\,\text{mm}^3$ were employed to measure the σ_{zr} versus γ_{zr} response,
(ii) the $\sigma_{z\theta}$ versus $\gamma_{z\theta}$ curve was obtained from specimens of dimension $20 \times 160 \times 16\,\text{mm}^3$ and
(iii) the $\sigma_{r\theta}$ versus $\gamma_{r\theta}$ curve was measured from specimens of dimension $20 \times 160 \times 16\,\text{mm}^3$.

Recall that the engineering shear strain is $\gamma_{ij} = 2\varepsilon_{ij}$, $i \neq j$. In all cases, the 160 mm and 16 mm sides defined the shear plane, with the shearing direction along the 160 mm side. Thus, consistent with the ASTM standard [12], an aspect ratio of ten was employed in the single-lap shear tests.

3.3.3. Experimental measurements

The measured compressive stress versus strain responses of balsa wood (density $90\,\text{kg}\,\text{m}^{-3}$) in the 4 directions detailed above are plotted in Fig. 2. All the curves display an initial elastic regime, a plateau regime and finally densification at a nominal densification strain of about 70–80%. The measured responses from tests (ii) to (iv) of Section 3.3.1 are nearly identical suggesting that balsa wood is isotropic in the $r-\theta$ plane. Moreover, in line with the findings of Easterling et al. [11], the stiffness and strength of balsa are seen to be much higher in the axial direction. The elastic Poisson's ratios were measured as $v_{13} \approx 0.1$ and $v_{12} \approx 0.2$, while nearly no lateral expansion was observed in the plastic range in any of the compression tests. This suggests that all the plastic Poisson's ratios satisfy $v^p_{ij} \approx 0$.

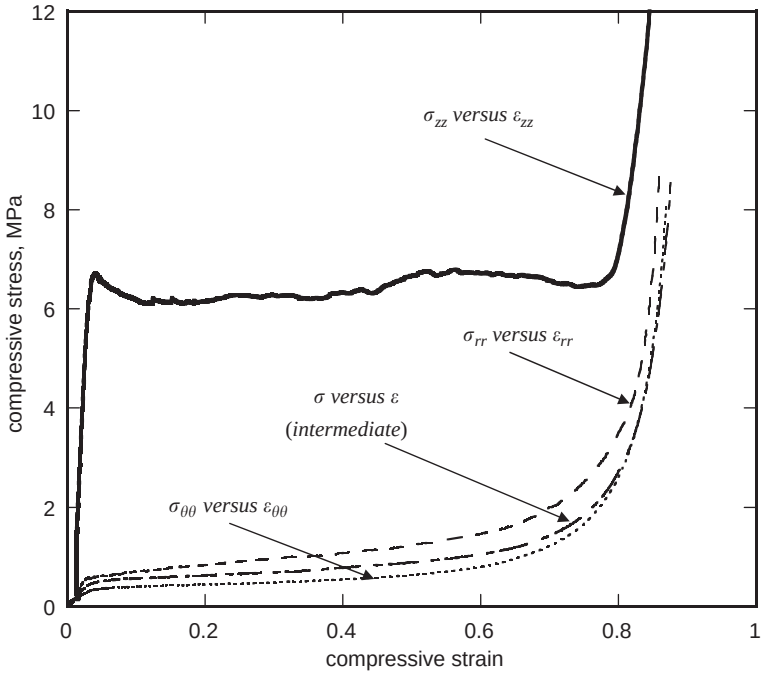

Fig. 2. Measured nominal compressive stress versus nominal compressive strain response of balsa (density 90 kg m^{-3}) in 4 directions. The intermediate direction refers to a uniaxial compression test in the $(r-\theta)$ plane in a direction at 45° to the r and θ directions.

The measured shear responses of balsa wood (density 130 kg m^{-3}) are plotted in Fig. 3. Again, in line with the anticipated isotropy of balsa wood in the $r-\theta$ plane, we observe that the $\sigma_{z\theta}$ versus $\gamma_{z\theta}$, and σ_{zr} versus γ_{zr}, curves are approximately equal with a peak shear strength of about 1.5 MPa. On the other hand, the balsa wood is much weaker when subjected to shear in the $r-\theta$ plane with a peak shear stress of about 0.5 MPa. Unlike the compressive response, the shear response of balsa does not include a long plateau followed by densification. Rather, the wood fractures at $\gamma^f_{z\theta} \approx \gamma^f_{zr} \approx 1\%$ and at $\gamma^f_{r\theta} \approx 3.5\%$.

These tests confirm that balsa is transversely isotropic. In the sequel, we shall refer to (r,θ,z) directions of balsa using the indices $(1,2,3)$, respectively, to be consistent with the notation of the transversely isotropic model of Section 2.

3.3.4. Scaling of properties with density

When balsa wood is loaded in the $r-\theta$ plane, the cell walls bend. Gibson and Ashby [1] treated the cells as a two-dimensional hexagonal array, and argued that the relevant elastic moduli and plastic yield strengths scale with density ρ according to the relations

$$E_{11} = E_{22} = \alpha_{11}\left(\frac{\rho}{\rho_0}\right)^3, \quad Y_{22} = Y_{11} = \beta_{22}\left(\frac{\rho}{\rho_0}\right)^2, \quad Y_{12} = \beta_{12}\left(\frac{\rho}{\rho_0}\right)^2, \tag{18}$$

where ρ_0 is a reference density and α_{ij} and β_{ij} are scaling constants that will be made explicit subsequently. On the other hand, the axial stiffness and strength of balsa wood is much larger as

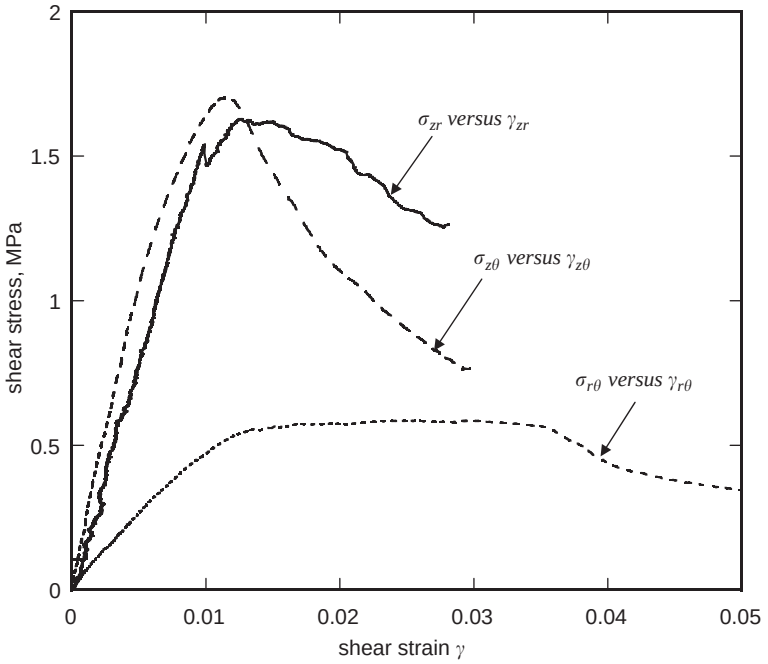

Fig. 3. Measured shear stress versus engineering shear strain curves of balsa wood (density $130\,\mathrm{kg\,m^{-3}}$) in three different planes.

in this direction the cell walls stretch rather than bend. In this case, the scaling with density follows the rule

$$E_{13} = E_{23} = \alpha_{13}\left(\frac{\rho}{\rho_0}\right), \quad E_{33} = \alpha_{33}\left(\frac{\rho}{\rho_0}\right),$$
$$Y_{33} = \beta_{33}\left(\frac{\rho}{\rho_0}\right), \quad Y_{13} = Y_{23} = \beta_{13}\left(\frac{\rho}{\rho_0}\right). \tag{19}$$

A series of tests were conducted on balsa wood specimens with densities in the range 70 to $130\,\mathrm{kg\,m^{-3}}$, to determine experimentally the scaling of the properties with density. While the elastic Poisson's ratios remained constant at $\nu_{13} \approx 0.1$ and $\nu_{12} \approx 0.2$, the moduli E_{11}, E_{33} and E_{13} were observed to scale with density according to Eqs. (18) and (19). The values of the scaling coefficients α_{ij} were determined by a least-squares fit of relations (18) and (19) to the experimental data. The values of α_{ij} with the reference density ρ_0 taken to be $100\,\mathrm{kg\,m^{-3}}$ are listed in Table 1. The associated average deviations of the experimentally measured moduli $E_{ij}^{(k)}$ from the least-squares fit is defined as

$$\Delta E_{ij} = \sqrt{\frac{\sum_{k=1}^{n}(E_{ij}^{(k)} - E_{ij})}{n^2}}, \tag{20}$$

where the superscripts $k = 1, \ldots, n$ denote the experimentally determined moduli. These deviations are also included in Table 1.

Table 1
The scaling coefficients α_{ij} determined by a least-squares fit to the experimental data for the elastic moduli and yield strengths, respectively. The root-mean-square deviations ΔE_{ij} of the experimental measurements from the least-squares fit are included. The reference density ρ_0 is taken to be $100\,\mathrm{kg\,m^{-3}}$

Subscripts ij	α_{ij} (MPa)	ΔE_{ij} (MPa)
11	76	10.87
33	845	95.48
13	80	9.68

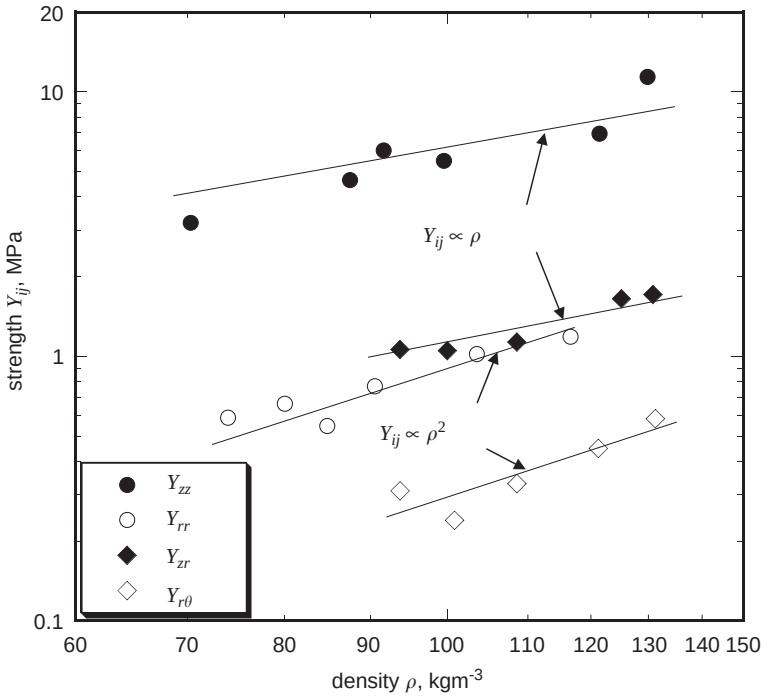

Fig. 4. Measured variation of the compressive and shear strengths of balsa wood with density. The lines through the data correspond to the scaling relations (18) and (19).

The experimentally measured variation of the plastic properties Y_{ij} with density is plotted in Fig. 4. In line with the scaling relations (18) and (19), we observe that the strengths Y_{11} and Y_{12} are proportional to ρ^2, while Y_{33} and Y_{13} scale linearly with ρ. Again, the coefficients β_{ij} were determined by a least-squares fit of the experimental data to Eqs. (18) and (19) and an average error in the strength ΔY_{ij} defined analogously to Eq. (20): both β_{ij} and ΔY_{ij} are listed in Table 2.

Table 2
The scaling coefficients β_{ij} determined by a least-squares fit to the experimental data for the elastic moduli and yield strengths, respectively. The root-mean-square deviations ΔY_{ij} of the experimental measurements from the least-squares fit are included. The reference density ρ_0 is taken to be $100\,\mathrm{kg\,m^{-3}}$

Subscripts *ij*	β_{ij} (MPa)	ΔY_{ij} (MPa)
22	0.95	0.093
33	6.50	0.610
12	0.30	0.026
13	1.25	0.120

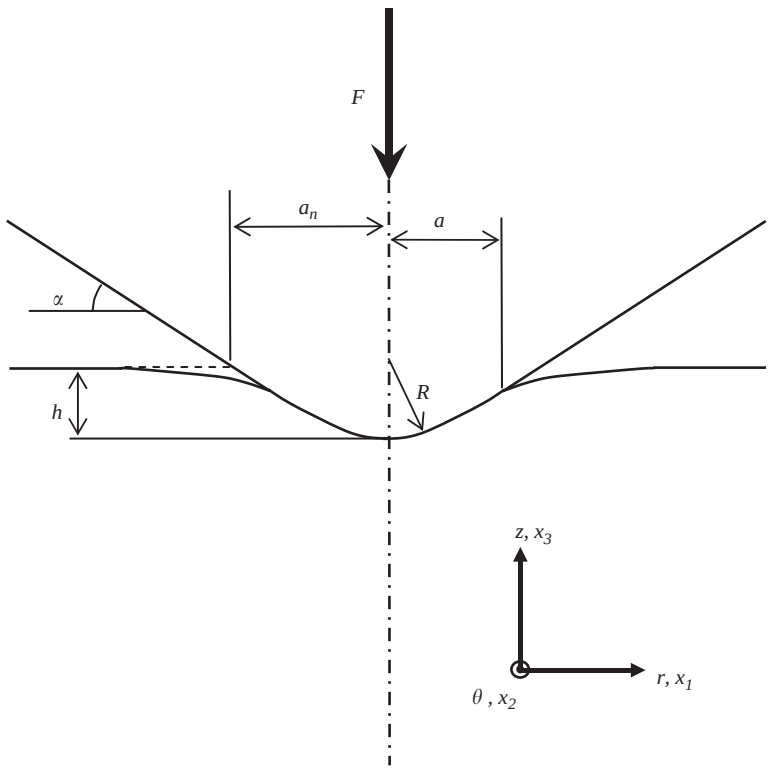

Fig. 5. Conical indentation of a balsa wood half-space, showing the notation and co-ordinate systems.

4. Indentation experiments

Indentation experiments by a cone have been performed on cuboidal balsa wood specimens measuring $35 \times 35\,\mathrm{mm^2}$ in the $r-\theta$ plane and 16 mm in the axial direction; the indentation direction was taken to be parallel to the axial (z) direction of the balsa wood as sketched in Fig. 5.

The indentation experiments were performed in a screw driven test machine at an indentation rate of $5 \times 10^{-3}\,\mathrm{mm\,s^{-1}}$, with the indentation load F measured by the load cell of the test machine and a laser extensometer used to measure the indentation depth h. Friction between the indenter and the specimens was minimised by lubricating in the indenter surface with a silicone spray. Conical indenters with side inclinations $\alpha = 20^\circ$, 30° and 60° were employed, see Fig. 5 for the definition of α. All the conical indenters had a spherically rounded tip with a tip radius $R = 3$, 2 and 0.6 mm for $\alpha = 20^\circ$, 30° and 60° cones, respectively. Balsa wood specimens of density 106, 87 and $98\,\mathrm{kg\,m^{-3}}$ were used in the $\alpha = 20^\circ$, 30° and 60° indentation experiments, respectively. Typically, indentation tests to a depth $h \leqslant 2$ mm were performed and the zone of indented balsa wood was observed to be much smaller than the specimen size. Thus, for all practical purposes, these experiments might be regarded as indentation into a half-space of balsa wood.

4.1. Experimental results

Scanning electron microscope (SEM) micrographs of the indented balsa wood specimens, sectioned along the diametral axis of the indenter, are shown in Figs. 6a and b for $\alpha = 20^\circ$ and 60°, respectively. The densified zone immediately below the indenter surface is clearly visible, with negligible permanent deformation outside the densified zone. The sap channels referred to in Section 3.1 are also visible in Fig. 6b. In order to develop a better understanding of the deformation mechanism, higher magnification SEM micrographs of the crush zone are shown in Fig. 7 for the $\alpha = 30^\circ$ case. The higher magnification photographs in Figs. 7b and c clearly show that indentation direction is parallel to the axis of the balsa wood tree trunk, with the prismatic hexagonal cells collapsing by a local buckling mechanism. Again, Figs. 7b and c confirm that negligible deformation occurs outside the densified zone.

The measured indentation force F versus displacement h curves are plotted in Figs. 8a–c for the $\alpha = 20^\circ$, 30° and 60° indenters, respectively. In all cases the force increases approximately quadratically with displacement. Furthermore, nearly no sink-in of the balsa wood was observed around the indented region suggesting that the actual contact radius a and the nominal contact radius a_n are approximately equal.

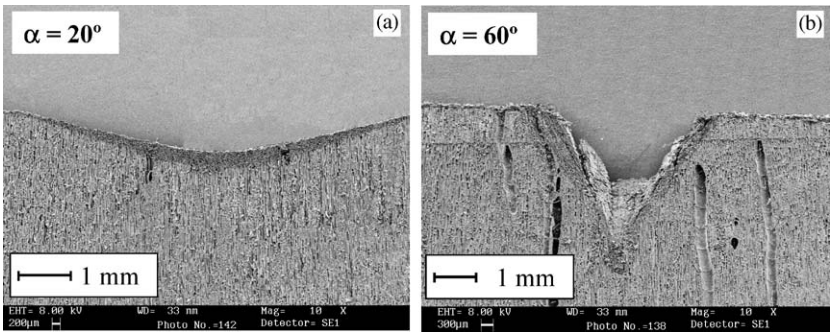

Fig. 6. SEM micrographs of the indented balsa wood specimens for (a) $\alpha = 20^\circ$ ($h \approx 0.8$ mm), (b) $\alpha = 60^\circ$ ($h \approx 2.2$ mm).

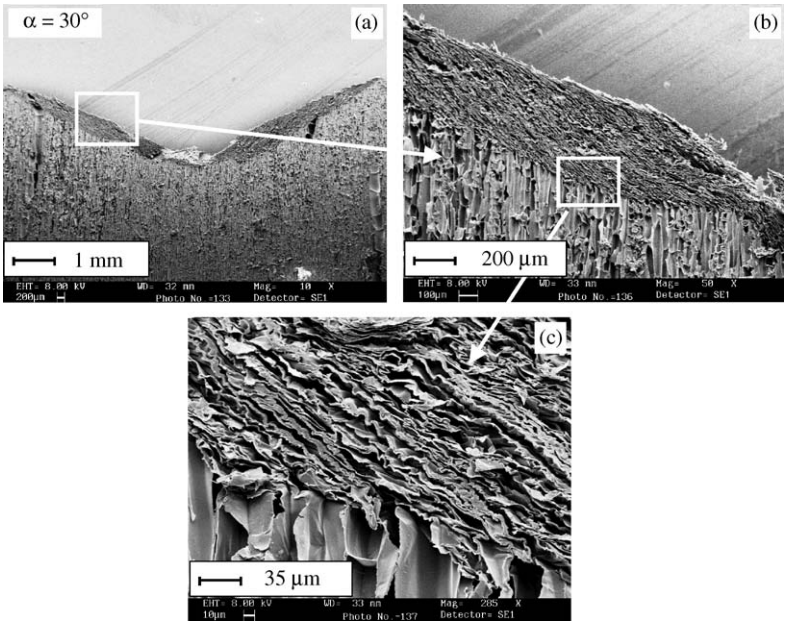

Fig. 7. SEM micrographs of the balsa wood specimen indented to a depth $h = 1.4$ mm with the conical indenter $\alpha = 30^\circ$. (a)–(c) are SEM micrographs with increasing magnification.

5. FE simulations

We proceed to discuss FE simulations of the indentation experiments described above. These FE simulations were performed to (i) develop an understanding of the mechanics of the indentation of balsa and (ii) to gauge the ability of the proposed transversely isotropic model to capture the indentation response of balsa wood.

The FE calculations of the indentation were performed using the general purpose FE package ABAQUS (HKS—*Hibbitt, Karlsson & Sorensen, Inc.*) with the balsa specimen ($35 \times 35 \times 16\,\text{mm}^3$) typically modelled by approximately 8000 reduced integration axisymmetric quadratic elements (the 8-noded CGAX8R element of ABAQUS). The base of the specimen was completely constrained (no vertical or horizontal displacements) while the lateral edges were taken to be traction free. Loading was applied through vertical prescribed displacements of a rigid conical indenter, with the contact between the cone and the upper surface of the specimen modelled by a frictionless contact surface as provided by ABAQUS. Note that the conical indenters used in the FE calculations had exactly the same geometry (i.e. same values of the spherical tip radius R and half-angle α) as those employed in the experiments.

For each indenter geometry, FE simulations were performed using two alternate constitutive descriptions for the balsa wood in the following manner:

(i) The balsa was modelled as an isotropic foam using the Deshpande and Fleck [7] constitutive law. The yield and hardening response of the foam was calibrated against the measured σ_{33}

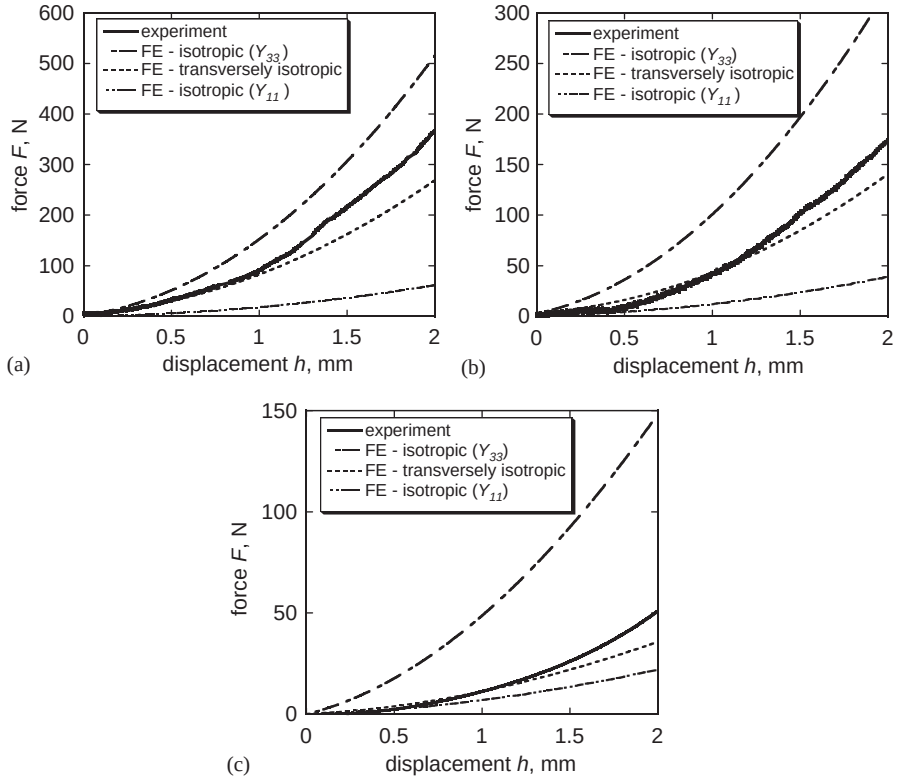

Fig. 8. Indentation force F versus displacement h for (a) $\alpha = 20^\circ$; (b) $\alpha = 30^\circ$; (c) $\alpha = 60^\circ$ conical indenters. The experimentally measured curves along with FE predictions of the isotropic and transversely isotropic foam models are included in the figures. Y_{11} and Y_{33} in the legend of the figures denote that the isotropic FE model is calibrated with the uniaxial σ_{11} versus ε_{11}^p and σ_{33} versus ε_{33}^p curves, respectively.

versus ε_{33}^p curve of balsa. Thus, the isotropic model is calibrated along the strongest direction of the balsa and this is expected to give an upper bound to the indentation resistance.

(ii) The balsa was modelled as an isotropic foam using the Deshpande and Fleck [7] constitutive law. The yield and hardening response of the foam was calibrated against the measured σ_{11} versus ε_{11}^p curve of balsa. Thus, the isotropic model is calibrated along the weakest direction of balsa, and this is expected to provide a lower bound to the indentation resistance.

(iii) The balsa was modelled as a transversely isotropic compressible solid using the constitutive law described in Section 2. The yield function and hardening response of the balsa were calibrated according to the procedure discussed in Section 2.2.

As discussed in Section 3.3.4, the mechanical properties of balsa are sensitive to its density. Moreover, as the commercial balsa sheets employed in this study comprised different blocks of balsa wood glued together, the density of the sheets is non-uniform. Thus, the FE models were calibrated by measuring the density of the balsa wood in the vicinity of the indented region and then employing relations (18) and (19) to determine the required input properties for the FE models.

5.1. Mesh sensitivity of the Fe calculations using the transversely isotropic model

The effect of mesh size on the FE predictions is illustrated in Fig. 9 for the choice $\alpha = 30^\circ$. Deformed meshes of about 1000 and 8000 elements are shown in Figs. 9a and b, respectively, for an indentation depth of $h = 1.5\,\text{mm}$. In both cases a kink-band-type instability is evident, with alternate layers of elements crushing. This instability is traced to the fact that $Y_{13} \ll Y_{33}$. It is clear from Figs. 9a and b that a reduction of the mesh size has no qualitative effect upon the observed deformation modes. This behaviour can be contrasted to the stable behaviour of isotropic foam under indentation; note that the shear strength is approximately equal to the compressive strength

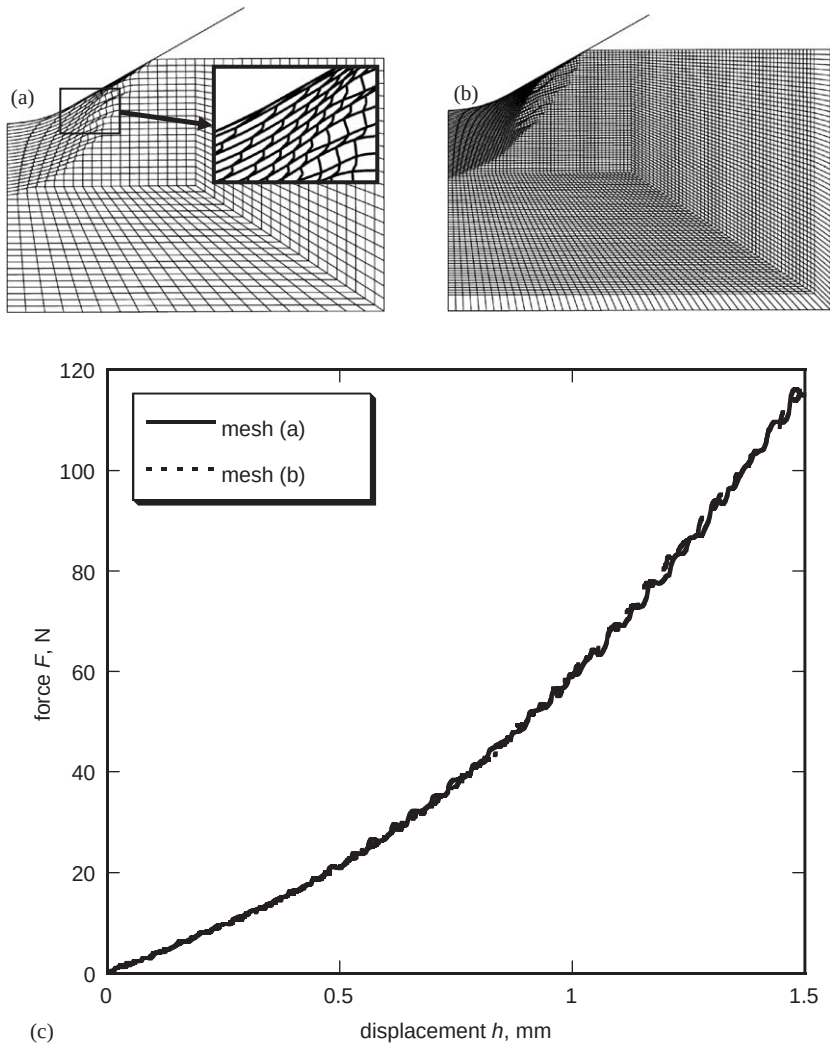

Fig. 9. Deformed FE (transversely isotropic foam model) meshes with (a) 1000 and (b) 8000 8-noded quadrilateral elements at an indentation depth $h = 1.5\,\text{mm}$ for $\alpha = 30^\circ$. The inset in (a) shows a magnified view of instability. (c) The effect of the mesh size on the FE predictions of the indention force F versus displacement h response.

for the isotropic solid. The effect of the mesh size upon the predicted indentation force versus displacement response is shown in Fig. 9c. The calculations of the force versus displacement history are almost independent of mesh size. All calculations reported below have been performed using the mesh shown in Fig. 9b.

5.2. Deformation mechanism

Define the normalised volumetric plastic strain rate by $\dot{\varepsilon}^p_m h/\dot{h}$, where $\dot{\varepsilon}^p_m \equiv \dot{\varepsilon}^p_{kk}$. Contours of $\dot{\varepsilon}^p_m h/\dot{h}$ are plotted in Figs. 10a and b for the choice $\alpha = 30^\circ$, at indentation depths of $h = 1$ and 1.8 mm, respectively. In both figures, the left-hand plot shows predictions using the isotropic foam model (calibrated using the σ_{33} versus ε^p_{33} curve) while the right-hand plot corresponds to the transversely isotropic model predictions. For both material descriptions, the mode of indentation is cavity expansion, as proposed by Johnson [13] for an incompressible isotropic solid and extended to a porous solid by Fleck et al. [14]. That is, the volumetric plastic strain rate is non-zero only in a narrow band, which encloses a region where the material is fully densified while outside this band, the material is elastic. This cavity of densified material expands in a self-similar

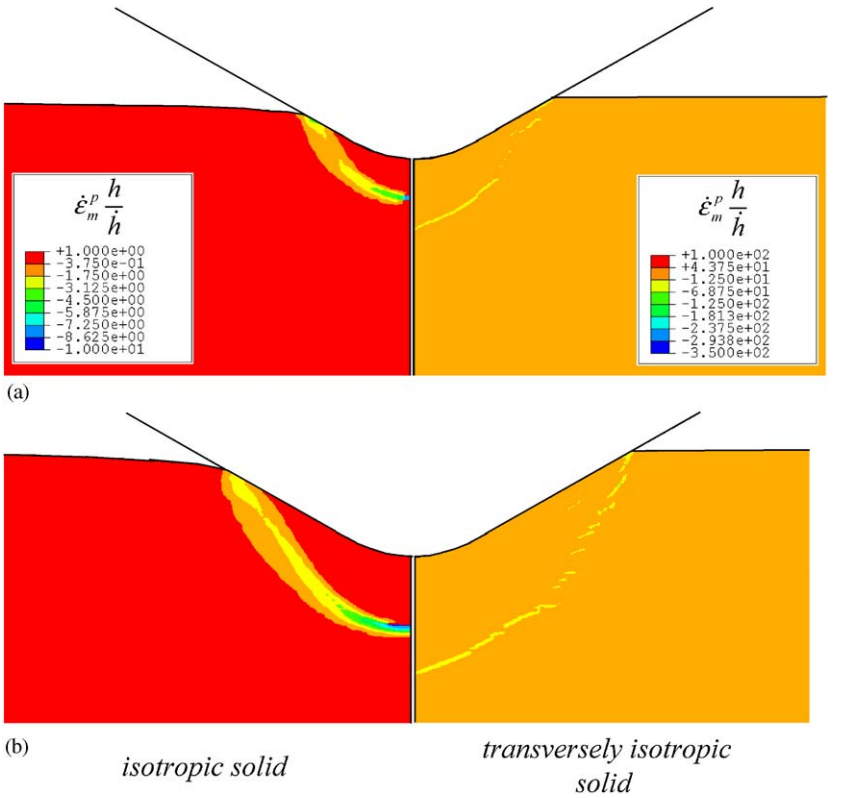

Fig. 10. Contours of the normalised volumetric plastic strain rate $\dot{\varepsilon}^p_m h/\dot{h}$ for $\alpha = 30^\circ$ case at two selected values of indentation depths: (a) $h = 1$ and (b) $h = 1.8$ mm. In both (a) and (b), FE predictions of the transversely isotropic and isotropic models are shown on the right- and left-hand sides, respectively.

manner with increasing indentation as described by Fleck et al. [14]. The main differences between the isotropic and transversely isotropic models are:

(i) The isotropic model predicts an approximately spherical cavity while the transversely isotropic model predicts a cavity more ellipsoidal in shape.
(ii) The isotropic model predicts sink-in around the indenter, which is not observed in the transversely isotropic model predictions, see Fig. 10. This observation is made explicit in Fig. 11, where the actual contact radius a predicted by the two sets of calculations is plotted as a function of the indentation depth h. Included in the figure, is the variation of the nominal contact radius a_n with indentation depth h as given by the geometric relation

$$a_n = \sqrt{R^2 - (R-h)^2} \quad \text{if } h < R(1-\cos\alpha)$$
$$= \frac{h-R}{\tan\alpha} + \frac{R}{\sin\alpha} \quad \text{otherwise.} \tag{21}$$

The figure clearly shows that, in line with the experimental observations, the transversely isotropic model predicts that $a \approx a_n$, while the isotropic foam model predicts sink-in with $a < a_n$ for any given value of h.

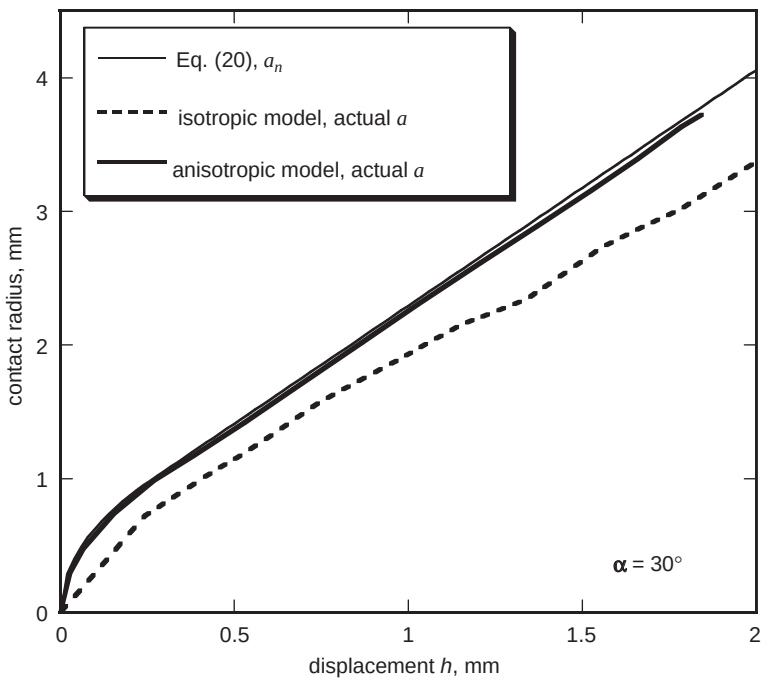

Fig. 11. FE predictions of the actual contact radius a as a function of the indentation depth for the $\alpha = 30°$ case. For comparison purposes, the variation of the nominal contact radius a_n with h is included in the figure.

6. Comparison between the FE predictions and experiments

Comparisons between the measurements and FE predictions of the indentation force F versus indentation depth h curves are given in Figs. 8a–c, for $\alpha = 20^\circ$, 30° and 60°, respectively. For each geometry, predictions are plotted for the three material laws described above. The isotropic foam model of Deshpande and Fleck [7], calibrated using the σ_{33} versus ε^p_{33} curve of balsa, over-predicts the indentation force for any given value of h while the isotropic model, calibrated with the σ_{11} versus ε^p_{11} curve of balsa, under-predicts the indentation force for the range of indentation depths considered here. We observe that the measured F versus h history is closer to the isotropic prediction employing the σ_{33} versus ε^p_{33} calibration curve for low values of the cone angle α, but is in better agreement with the isotropic prediction employing the σ_{11} versus ε^p_{11} calibration curve for higher values of α. This is rationalised by noting that in the limit $\alpha \to 0$, indentation occurs by the uniaxial compression of the balsa in the 3 direction as the plastic Poisson's ratio $v^p_{13} \approx 0$. Thus, the indentation response is governed by the σ_{33} versus ε_{33} response of balsa wood. On the other hand, with increasing α, the lateral strength of the balsa wood Y_{11} becomes increasingly important, resulting in better agreement with the isotropic foam model using the σ_{11} versus ε^p_{11} calibration curve.

The FE predictions employing the transversely isotropic foam model agree well with the experimental measurements for indentation depths $h < 1.2$ mm for all values of α considered in this study. In the later stages of the indentation, the measured and predicted responses tend to diverge, with the transversely isotropic FE model under-predicting the measured load.

In order to gauge the effect of the cone angle on the indentation response we proceed to quantify the effect of α on the measured and predicted values of mean indentation pressure, as averaged over the indentation depth. The mean indentation pressure is defined as

$$p = \frac{1}{h_2 - h_1} \int_{h_1}^{h_2} \frac{F}{\pi a^2} \, \mathrm{d}h \tag{22}$$

and we shall average the pressure over indentation depths in the range $h_1 = 0.5$ mm to $h_2 = 1.8$ mm. Here, a is the actual contact radius, and has been extracted from FE simulations as a function of the indentation depth h. The FE predictions of p using the three material models discussed above have been normalised by the axial strength of the balsa wood Y_{33}, and are plotted in Fig. 12 for the three cone angles considered. It is evident that the predicted mean indentation pressure p, increases with α, consistent with the findings of Fleck et al. [14] for the indentation of a porous solid. The experimental observations confirm the FE predictions that the nominal contact radius a_n is approximately equal to the actual contact radius a. Excellent agreement is observed between the measured and predicted values of the mean indentation pressure by the transversely isotropic model. On the other hand, the isotropic foam model is unable to predict the indentation pressure over the full range of α.

7. Concluding remarks

The Deshpande and Fleck [7] model for isotropic foams has been extended to transversely isotropic compressible solids. A quadratic yield surface is proposed, with four plasticity

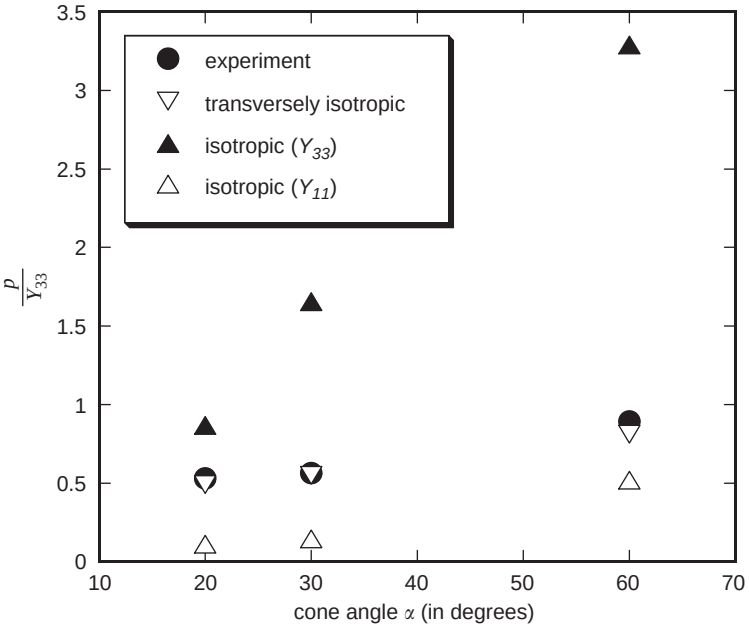

Fig. 12. Experimental measurements and FE predictions of the indentation pressure p for the three cone angles considered here. Y_{11} and Y_{33} in the legend of the figure denote that the isotropic model FE is calibrated with the uniaxial σ_{11} versus ε_{11}^p and σ_{33} versus ε_{33}^p curves, respectively.

parameters and one hardening function, to be set by the user. Associated plastic flow is assumed and the yield surface is constrained to evolve in a self-similar manner, calibrated by the uniaxial compressive (or tensile) response of the foam in the axial direction. In principle, all the material constants in the model (elastic and plastic) can be determined from a combination of two uniaxial and shear tests.

Indentation tests on balsa wood have been conducted to investigate the validity and applicability of the proposed transversely isotropic foam model. First, a series of compressive and shear tests on commercial balsa wood were performed. These tests confirmed that for all practical purposes balsa wood may be considered as a transversely isotropic foam. Next, conical indentation tests in the axial direction, with three cone geometries were conducted. FE simulations of these experiments using the new transversely isotropic foam model and the isotropic Deshpande and Fleck [7] foam model were performed. Good agreement is seen between the predictions of the transversely isotropic model and the experimental measurements for all cone geometries considered here. On the other hand, the isotropic model is unable to capture the indentation response.

The transversely isotropic foam model developed here is able to capture the indentation response of balsa wood. A variety of new lattice materials have been developed recently for sandwich core applications; these materials include the pyramidal core and square-honeycomb core, and they also fall into the category of transversely isotropic cellular solids. The applicability of the proposed model for such lattice materials is a topic for future study.

Acknowledgements

This work was supported by the US Office of Naval Research, Contract No. 0014-91-J-1916.

References

[1] Gibson LJ, Ashby MF. Cellular solids, structure and properties, 2nd ed. Cambridge: Cambridge University Press; 1997.
[2] Deshpande VS, Fleck NA, Ashby MF. Effective properties of the octet-truss lattice material. Journal of the Mechanics and Physics of Solids 2001;49(8):1747–69.
[3] Zupan MP, Fleck NA. Compressive response of the pyramidal core lattice material. 2004, in preparation.
[4] Cote F, Deshpande VS, Fleck NA, Evans AG. The out-of-plane compressive behaviour of metallic honeycombs. Material Sciences and Engineering A 2004;380:272–80.
[5] Triantafillou TC, Gibson LJ. Constitutive modelling of elastic-plastic open-cell foams. Journal of Engineering Mechanics 1990;116:2772–8.
[6] Hill R. A theory of the yielding and plastic flow of anisotropic materials. Proceedings of the Royal Society of London 1947;A193:281–97.
[7] Deshpande VS, Fleck NA. Isotropic constitutive models for metallic foams. Journal of the Mechanics and Physics of Solids 2000;48:1253–83.
[8] Xue Z, Hutchinson JW. Constitutive model for quasi-static deformation of metallic sandwich cores. International Journal of Numerical Methods in Engineering 2004;61(13):2205–38.
[9] Lubliner J. Plasticity theory. London: Macmillan; 1990.
[10] Chen C, Deshpande VS, Fleck NA. A constitutive model for a transversely isotropic compressible solid: user manual for a UMAT in ABAQUS. Cambridge University Engineering Department internal report, CUED/C-MICROMECH/TR.93, 2003.
[11] Easterling KE, Harrysson R, Gibson LJ, Ashby MF. On the mechanics of balsa and other woods. Proceedings of the Royal Society of London 1982;A383:31–41.
[12] ASTM Standard C273-94. Standard test method for shear properties of sandwich core materials. American Society for Testing and Materials, 1994.
[13] Johnson KL. Contact mechanics. Cambridge: Cambridge University Press; 1985.
[14] Fleck NA, Otoyo H, Needleman A. Indentation of porous solids. International Journal of Solids and Structures 1992;29:1613–36.